Article

Not peer-reviewed version

Experimental and Numerical Investigation on the Formation Mechanism of Freckle Defects in a Novel Third-Generation Nickel-Based Single Crystal Superalloy Turbine Blade

Xiaoshan Liu , Anping Long , Haijie Zhang * , Dexin Ma , Min Song , Menghuai Wu , Jianzheng Guo *

Posted Date: 10 March 2026

doi: 10.20944/preprints202603.0714.v1

Keywords: nickel-based single crystal superalloy; freckle defects; directional solidification; numerical simulation; turbine blade

Article

Experimental and Numerical Investigation on the Formation Mechanism of Freckle Defects in a Novel Third-Generation Nickel-Based Single Crystal Superalloy Turbine Blade

Xiaoshan Liu [1,2], Anping Long [2], Haijie Zhang [3,*], Dexin Ma [1,2], Min Song [1], Menghuai Wu [4] and Jianzheng Guo [1,2,*]

[1] State Key Laboratory of Powder Metallurgy, Central South University, Changsha 410083, China
[2] Shenzhen Wedge Central South Research Institute Co., Ltd., Shenzhen 518045, China
[3] School of Mechanical and Materials Engineering, North China University of Technology, Beijing, 100144, China
[4] Department of Metallurgy, University of Leoben, A-8700 Leoben, Austria
* Correspondence: haijie.zhang@ncut.edu.cn (H.Z.); 218062@csu.edu.cn (J.G.)

Abstract

This paper investigates the formation mechanism and key influencing factors of freckle defects that arise during the directional solidification of a novel third-generation nickel-based single crystal superalloy turbine blade. A combined experimental and multi-physics numerical simulation approach was adopted. The results indicate that freckle formation primarily originates from solutal convection, which subsequently triggers a cascade of processes, including the development of convection-induced segregation channels, flow-driven dendrite fragmentation, and the migration and aggregation of dendrite fragments. The severity of freckling is closely dependent on both the casting's position within the furnace and its local geometric characteristics. Castings located in regions with poorer heating conditions exhibit lower temperature gradients and slower solidification rates, significantly increasing their susceptibility to freckle formation. Similarly, on a given casting, the side subjected to less favorable heating is more prone to freckle initiation. This study provides a crucial theoretical basis for understanding the formation mechanism of freckle defects in nickel-based single crystal superalloys and offers valuable guidance for optimizing blade manufacturing processes, reducing solidification defects, and enhancing blade quality and service performance.

Keywords: nickel-based single crystal superalloy; freckle defects; directional solidification; numerical simulation; turbine blade

---

1. Introduction

Nickel-based single crystal superalloys are the core materials for manufacturing turbine blades in advanced aeroengines and heavy-duty gas turbines, and their temperature capability directly determines the power and efficiency of the engines [1,2]. With the continuous increase in thrust-to-weight ratio requirements in the aviation industry, the turbine inlet temperature has exceeded 1650 °C, posing extremely stringent challenges to the high-temperature performance of these alloys. Third-generation nickel-based single crystal superalloys have significantly enhanced high-temperature strength and creep resistance through the addition of high levels of refractory elements (e.g., 3–6 wt.% Re and 5–8 wt.% W). However, this increased alloying also intensifies the tendency for macrosegregation during solidification, leading to a variety of solidification defects, among which freckle defects are a typical example [3,4].

During the directional solidification process for manufacturing single crystal blades, freckle defects represent a typical and detrimental macroscopic solidification defect. These defects are typically distributed in chains along the gravity direction, consisting of strings of fine equiaxed grains and often accompanied by localized eutectic enrichment [5–9]. The presence of freckles compromises the single crystal integrity of the casting, significantly degrading the high-temperature mechanical properties and fatigue life of the blade. Since such defects cannot be eliminated by subsequent heat treatment, they frequently lead to high rejection rates of blades, making them a critical bottleneck restricting the yield improvement of high-performance single crystal blades.

Since the 1970s, freckle defects have received systematic attention. Copley et al. [10–12] were the first to systematically describe their morphology and characteristics. Subsequently, numerous studies have explored their formation mechanism using industrial superalloys [13–15] or model alloys (e.g., Pb-Sn, Pb-Sb [16], and $NH_4Cl–H_2O$ [17]). It is widely accepted that freckles originates from thermo-solutal convection within the mushy zone: the interdendritic liquid, enriched with low-density solute elements such as Al and Ti, undergoes density inversion, triggering upward flow that washes away and remelts dendrite arms, ultimately leading to the formation of equiaxed grain chains [18]. It was reported that higher cooling rates and temperature gradients are generally conducive to suppressing freckle defects [19,20]; however, this simple rule is not universally applicable to all castings [21]. In recent years, Ma et al. [14,22,23] have systematically revealed through experiments the influence of turbine blade geometry on freckle formation, proposing various mechanisms such as the “edge effect,” “shadow effect,” “step effect,” “curvature effect,” and “crystal orientation effect.” However, in actual blades, because multiple effects often intertwine and coexist, identifying the dominant mechanism remains challenging.

With the advancement of numerical simulation techniques, researchers have begun to explore the formation mechanism of freckles in depth from the perspective of multi-physics and multiphases coupling. Beckermann et al. [24,25] established a macroscopic transport model considering thermo-solutal convection, proposed a Rayleigh number-based criterion for freckle formation, and achieved effective prediction of freckle distribution in castings with simple geometries. However, for actual turbine blades with complex internal cavity structures, traditional models still struggle to achieve accurate predictions. This difficulty stems from the fact that the blade geometry significantly perturbs the temperature and solute fields at the solidification front, inducing local heat flux anomalies and solute enrichment, which in turn affect defect initiation and evolution. Although some models that directly resolve dendrite morphology at the microscale [26,27] can effectively reveal the initiation mechanism of freckles, their computational cost is extremely high. They are only applicable to locally simplified geometric regions and have difficulty coupling global thermal factors such as radiation and shading within the Bridgman furnace, making them unsuitable for full-blade simulations at an engineering scale. Recent studies indicate that solidification models based on the volume-averaged method are more promising for such problems [28,29]. By averaging microscopic phenomena, this method achieves effective coupling with macroscopic transport processes and has demonstrated good capability and computational efficiency in predicting freckle initiation and evolution [30,31].

In industrial production, turbine blades are typically cast in clusters by arranging multiple blades into a circular mold assembly within a Bridgman furnace. Due to the significant shading effect inside the furnace, considerable temperature differences arise among blades positioned at different orientations, with measured variations reaching approximately 20 K [32]. Experimental observations indicate that regions of the blade facing away from the heat source are more susceptible to freckle formation, whereas areas facing the heating zone remain nearly free of such defects [32]. Furthermore, the ceramic cores used to form the internal cavities of hollow blades further increase the complexity of the thermal and flow fields during solidification [33–35].

The present study investigates the formation characteristics of freckle defects during the directional solidification of a novel third-generation nickel-based single-crystal superalloy turbine blade under industrial casting conditions. Casting experiments were conducted in a Bridgman furnace, and the freckles in the as-solidified blades were systematically characterized, with particular emphasis on the freckle morphology and the grain structures in the vicinity of the freckles. The freckling tendency of turbine blades located at different positions within the furnace was compared to evaluate the influence of thermal–flow conditions on defect formation. In addition, a correlation analysis between local solidification conditions and freckle formation was performed using the Rayleigh number criterion. Finally, based on the solidification process characteristics obtained from the digital twin simulation framework previously developed by the authors [28,36], the freckle formation mechanism is discussed by considering the interaction between interdendritic flow and solidification behavior.

2. Experimental and Numerical Methods

2.1. Casting Preparation and Characterization

This study investigates a novel third-generation nickel-based single crystal superalloy, and its nominal chemical composition is presented in Table 1. Single crystal turbine blades were fabricated using the spiral grain selector method in a directional solidification furnace. The freckle defects formed in the as-cast microstructure of the blades were characterized and analyzed.

Table 1. Chemical composition of the investigated superalloy (wt.%).

Element	Al	Co	Cr	Fe	Hf	Mo	Nb	Re	Ta	Ti	W	Ni
Content	5.69	5.97	3.39	0.21	0.03	0.41	0.10	4.89	8.07	0.15	6.52	Base

Molds were prepared using alumina-based ceramic shells, with each shell assembly accommodating nine castings to ensure experimental efficiency and data consistency. The single crystal turbine blades were cast and directionally solidified in a VIM-IC/DS/SC Bridgman vacuum directional solidification furnace manufactured by ALD, which is equipped with precise temperature control capabilities. The thermal zone configuration and the spatial arrangement of the shell assembly are illustrated in Figure 1(a).

The specific process steps are as follows: Prior to pouring, the ceramic shell was transferred to the furnace's preheating chamber and preheated to a holding temperature precisely controlled at 1723 ± 5 K. After the alloy charge was completely melted, the melt was poured into the preheated ceramic shell at the same temperature of 1723 ± 5 K. Following the pouring, the shell assembly was withdrawn from the hot zone (1723 ± 5 K) into the cold zone (353 ± 2 K) at a rate of 1.5 mm/min to trigger the directional solidification process.

After the directional solidification process, the mold assembly was removed from the furnace, and the shell was eliminated. The casting system was removed using a precision cutting machine.. To examine the single crystal integrity and freckle defects, the castings were first subjected to macro-etching using an etchant with a composition of $CuSO_4 : HCl : H_2O$ = 4 g : 10 mL : 20 mL. Freckle defects and other grain defects were identified and marked through this macro-etching method. Subsequently, cross-sectional samples were sectioned from the blade airfoil using a wire electrical discharge machine. These samples were sequentially mounted, ground, polished, and chemically etched using the same etchant formulation. The microstructure was observed using an MM-400 optical microscope. A schematic diagram of the casting gating system model and the investigated castings are shown in Figure 1.

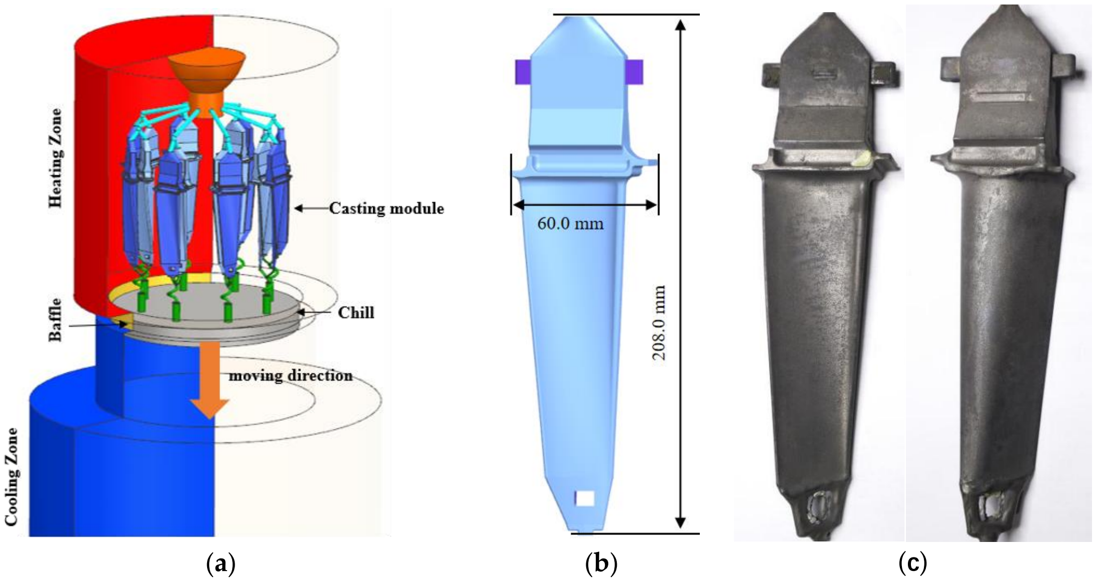

Figure 1. Schematic of the casting assembly in a Bridgman furnace and an example of superalloy single-crystal turbine blade: (a) Gating system assembly; (b) Geometry and dimensions of the blade; (c) Surface morphology of a as-cast single-crystal turbine blade.

2.2. Numerical Calculation Model and Method

2.2.1. Temperature Field Calculation

Figure 1(a) illustrates the full-scale geometric model of the gating system in the Bridgman furnace. A 1/9 symmetry model was adopted for simulation, as shown in Figure 2(a). The system consists of an upper heating zone and a lower cooling zone separated by an insulating baffle. The ceramic shell mold is placed on a water-cooled copper chill plate, with a ceramic core embedded to form the internal cavity of the turbine blade. Directional solidification is achieved by withdrawing the mold assembly downward at a constant rate.

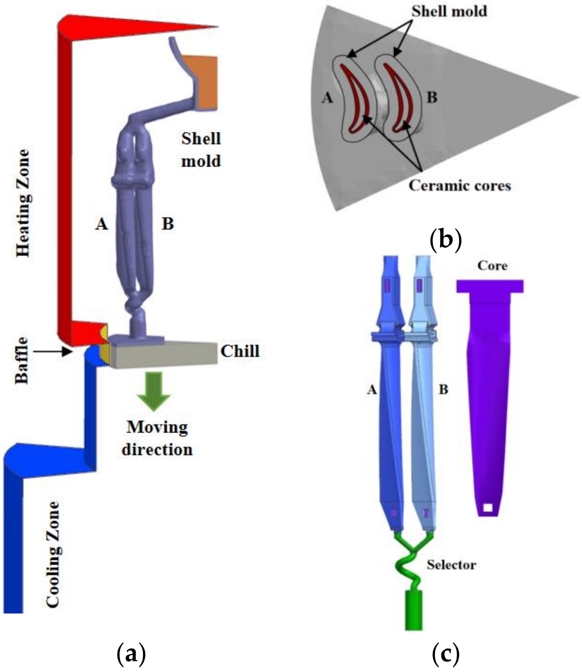

Figure 2. Numerical model for temperature field calculation: (**a**) Schematic diagram of the mold and casting assembly positioned in the Bridgman furnace; (**b**) Cross-sectional schematic of the casting within the ceramic shell; (**c**) Geometry of the casting and ceramic core.

Temperature field simulation was performed using the commercial software ProCAST. The geometric models of the turbine blade, ceramic core, and ceramic shell are shown in Figure 2(b) and (c), respectively. In the model, the relative lifting motion of the furnace body was used to simulate the dynamic displacement between the shell and the furnace. The calculated temperature field data will serve as the initial and boundary conditions for the subsequent flow-solidification coupling analysis using the ANSYS Fluent software.

2.2.2. Flow-Solidification Coupling Calculation

To describe the solidification process in the casting, a numerical framework based on a multiphase volume-averaged solidification model was employed, and the thermal field transfer scheme is illustrated in Figure 3. To couple the furnace-scale thermal field with the local solidification behavior of the turbine blade, a global–local digital twin strategy previously developed was adopted [36]. In the first step, the global temperature field of the Bridgman furnace, including the casting system, was calculated using ProCAST. In the second step, the flow and solidification processes inside the turbine blade were simulated using the multiphase volume-averaged solidification model. The temperature history on the blade surface obtained from the ProCAST simulation was then mapped onto the local model to provide thermal boundary conditions. The method for transferring thermal data between the two simulations is illustrated in Figure 3(c) to (e). Temperature histories were extracted from predefined locations on the blade surface in the ProCAST model (blue points) and expressed as fitted temperature–time functions. In the local solidification model, temperatures at the centroids of computational cells (red points) were obtained by bilinear interpolation from the surrounding surface data points. The interpolated temperature histories were subsequently implemented through a user-defined function as thermal boundary conditions for the flow–solidification calculations.

Owing to the high computational cost of fluid-flow simulations, only Casting B was considered in the coupled flow–solidification calculations. The computational domain of the volume-averaged solidification model was restricted to the blade body region (Figure 3(b)). The governing equations include the conservation of mass, momentum, energy, and solute for the multiphase system, enabling the simulation of melt convection, permeability evolution within the mushy zone, and thermo-solutal convection during solidification. Further details of the model formulation are provided in Ref. [36].

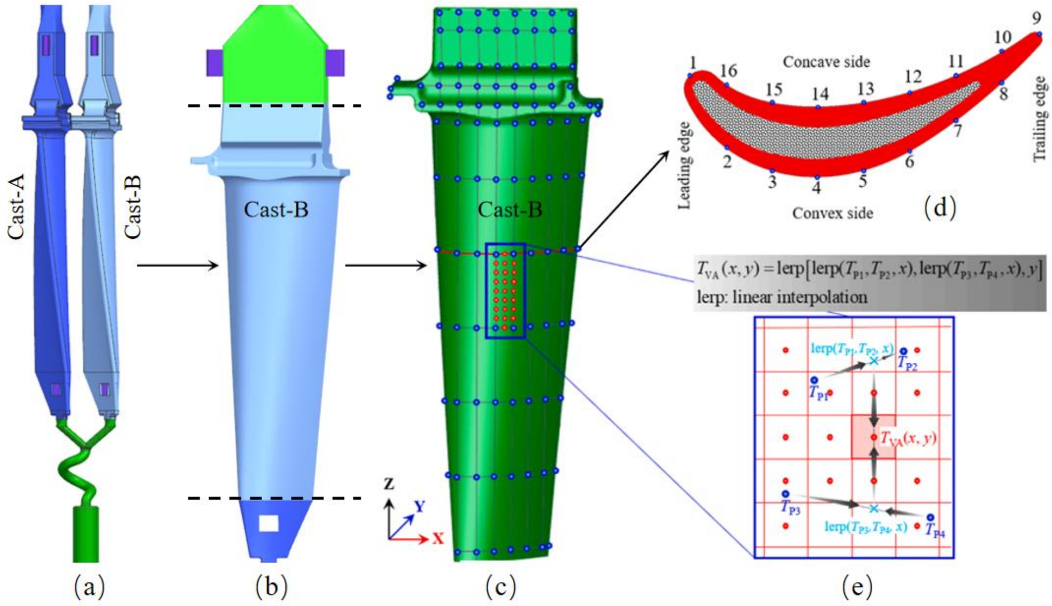

Figure 3. Schematic of the thermal coupling procedure between ProCAST and the volume-averaged solidification model: (**a**) Geometric model of the casting assembly in the Bridgman furnace; (**a**) The casting body (blue region) and its position within the assembly; (**a**) Spatial distribution of temperature extraction points in

ProCAST (blue dots) and interpolation points in the volume-averaged model (red dots) [36]; (**a**) Distribution of surface extraction points at the cross-section Z = 0.18 m [36]; (**a**) Schematic of the bilinear interpolation scheme for data transfer between two models [36].

The alloy melt was treated as an incompressible fluid with constant density and viscosity. To balance computational cost and accuracy, the multicomponent superalloy was approximated as an equivalent binary alloy system to represent its solidification behavior. Regions susceptible to freckle formation were evaluated using the solute enrichment index. The key material properties and processing parameters used in the simulations are summarized in Table 2 [36].

Table 2. Material properties and processing parameters [36].

Properties/parameters	Symbol	Units	Values
Thermophysical			
Specific heat of the alloy	$c_{p,l}$; $c_{p,s}$	J·kg^{-1}·K^{-1}	500.0
Latent heat	Δh_f	J·kg^{-1}	2.4×10^{5}
Liquid diffusion coefficient	D_1	m^{2}·s^{-1}	3.6×10^{-9}
Liquid thermal conductivity	k_1	W·m^{-1}·K^{-1}	33.5
Solid thermal conductivity	k_s	W·m^{-1}·K^{-1}	24.6
Thermal expansion coefficient	β_T	K^{-1}	-1.16×10^{-4}
Solutal expansion coefficient	β_c	wt.%$^{-1}$	-0.228
Density	ρ	kg·m^{-3}	7646.0
Viscosity	μ_1	kg·m^{-1}·s^{-1}	4.9×10^{-3}
Thermodynamic			
Eutectic temperature	T_{eut}	K	1627.0
Liquidus slope	m	K (wt. %)$^{-1}$	-1.145
Equilibrium partition coefficient	k	-	0.57
Primary dendritic arm spacing	λ_1	μm	500.0
Melting point of the solvent	T_f	K	1728.0
Others			
Initial concentration	$\bar{C}_0$	wt.%	35.09
Initial temperature	T_0	K	1773.0
Withdrawal velocity	v	mm/min	3.0

3. Experimental Results and Analysis of Freckle Defects

3.1. Macroscopic Characteristics of Freckles in Castings at Different Furnace Positions

Two nickel-based superalloy turbine blade castings (designated as Casting A and Casting B), prepared under identical conditions with consistent dimensions, were selected as the research objects. Their positioning within the furnace is illustrated in Figure 2. Casting A, positioned adjacent to the heating element, was defined as the hot zone casting; Casting B, positioned away from the heat source, was defined as the cold zone casting.

To elucidate the macroscopic distribution characteristics of freckle defects on the outer surfaces of the two castings, a visual inspection method was employed to qualitatively document the distribution locations, morphological features, size ranges, and number density of the defects. The specific procedure was as follows: after etching, the entire surface of the casting was observed under natural light conditions. The positions of freckle defects visible to the naked eye were marked, and their macroscopic distribution patterns and aggregation tendencies were systematically recorded. This provided foundational data to subsequent analysis of defect formation causes.

3.1.1. Distribution of Freckles on the Outer Surface of Casting A

Figure 4 illustrates the macroscopic distribution of freckles on the outer surface of Casting A. Detailed observations revealed that freckle defects were present exclusively on the convex side (Figure 4(a), (b)), while no freckle defects were observed on the concave side (Figure 4(c)). Figure 4(d) presents a schematic diagram of the freckle distribution on the convex side. Following a previous work of the authors [28], freckles were distinguished from segregation channels by the presence of stray grains. A segregation channel is defined as a freckle only when spurious grains are present; otherwise, it is termed a quasi-freckle. Regions marked by orange lines represent segregation channels, appearing as continuous traces with uniform coloration, where abundant eutectic aggregates were observed under metallographic microscopy. Regions marked in red represent stray grains, appearing as dotted or patchy discoloration in the form of intermittent traces, which constitute the core manifestation of freckle defects. For ease of description, as depicted in Figure 4(d), the three freckle traces on the convex side were designated as Freckle-I, Freckle-II, and Freckle-III.

Freckle-I originated at the bottom of the turbine blade, with its trace line predominantly consisting of segregation channels (marked by orange lines). After extending above the platform, stray grains (marked by red lines) appeared within the segregation channels, indicating the transformation into freckle defects in this region. Along the solidification direction, Freckle-I shows a clear incubation stage and subsequently develops within eutectic-enriched segregation channels, indicating a strong correlation between freckle formation and eutectic segregation. Unlike Freckle-I, both Freckle-II and Freckle-III formed directly in the fir-tree root region without an obvious incubation stage of segregation channels, presenting predominantly as stray grains in the form of dotted or patchy discoloration.

(a) (b) (c) (d)

Figure 4. Macroscopic distribution of freckle defects on the outer surface of Casting A: (**a**) Convex side; (**b**) Enlarged view of the convex side; (**c**) Concave side; (**d**) Schematic diagram of freckle defect distribution on the convex side (red lines: freckle defects/stray grains; orange lines: segregation channels/eutectic-rich regions.

3.1.2. Distribution of Freckles on the Outer Surface of Casting B

Figure 5 illustrates the macroscopic characteristics of freckle defects on the outer surface of Casting B. Observations reveal that freckle defects on this blade are also exclusively distributed on the convex side (Figure 5(a), (b)), with no defects observed on the concave side (Figure 5(c)). For ease of description, the seven freckle traces on the convex side are sequentially designated as Freckle-I through Freckle-VII, as shown in Figure 5(d), where orange lines indicate segregation channels and red lines indicate stray grains.

Freckle-I disappears from the blade surface after extending only a short distance, with some of its internal stray grains subsequently evolving into coarse misoriented dendrites (i.e., sliver defects). Freckle-II originates near the bottom of the turbine blade. In the lower airfoil region, it appears as segregation channels (orange lines). As solidification proceeds upward, these channels gradually evolve into freckles containing stray grains in the middle and upper airfoil regions, appearing as dotted or patchy discoloration. This transition is attributed to the increasing flow intensity within the segregation channel. In the lower blade region, the relatively small thickness results in weak interdendritic flow, and the defect mainly appears as segregation channels. With increasing blade thickness along the solidification direction, the flow intensity increases, enhancing dendrite arm remelting and fragmentation and promoting the formation of misoriented grains within the channel. Consequently, Freckle-I, III, and IV form directly in the upper part of the airfoil region without developing a long segregation-channel tail.

Furthermore, Freckle-II, III, and IV, located on the airfoil, disappear from the surface when extending near the platform, with no freckle defects observed in the platform region. Notably, as the blade cross-section exhibits a pattern of "contraction-expansion-recontraction" along the solidification height, the distribution of freckle defects correspondingly presents a characteristic of "appearance-disappearance-reappearance." This phenomenon is consistent with findings from our previous studies [14], namely that freckle defects do not appear immediately after cross-section expansion but gradually emerge after a brief incubation period.

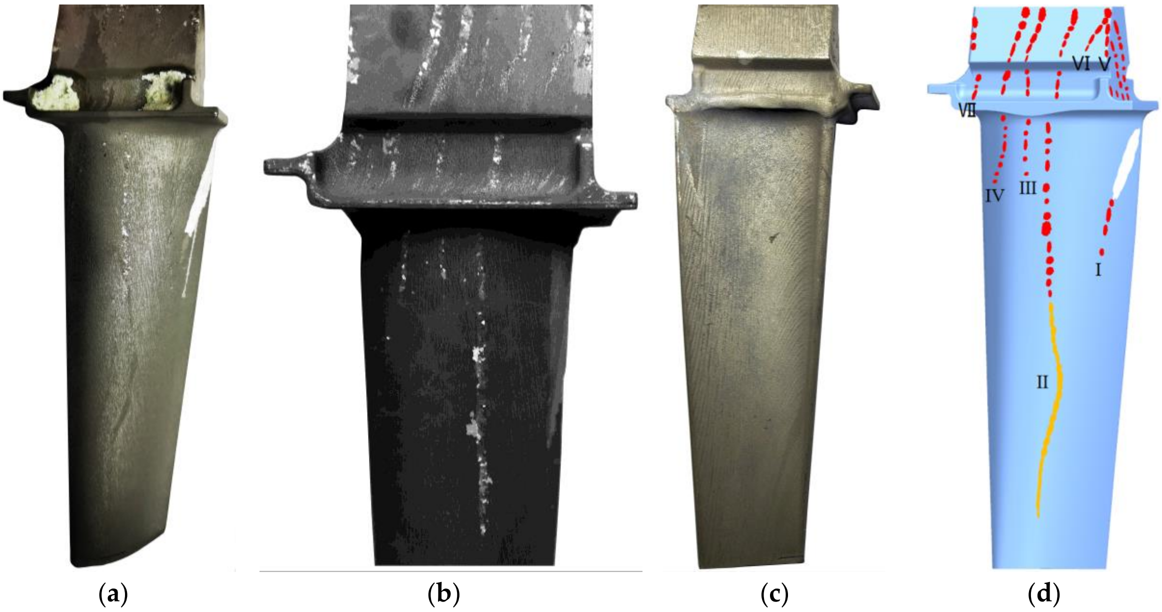

Figure 5. Macroscopic distribution of freckle defects on the outer surface of Casting B: (**a**) convex side; (**b**) Enlarged view of the convex side; (**c**) Concave side; (**d**) Schematic diagram of freckle defect distribution on the convex side (red lines: freckle defects/stray grains; orange lines: segregation channels/eutectic-rich regions.

3.2. Metallographic Analysis of Typical Freckle Defect Regions in Casting B

Based on the preceding observations of the macroscopic distribution characteristics of freckle defects on Casting B. Three typical regions were selected for metallographic analysis: the segregation channel region of Freckle-II, the transition region between the segregation channel and stray grains, and the initiation region of Freckle-V above the platform.

3.2.1. Metallographic Characteristics of the Segregation Channel Region of Freckle-II

An Olympus GX71 metallographic microscope was employed to observe the microstructure of specimens after grinding, polishing, and etching. The analysis focused on the microscopic morphology, grain structure, eutectic aggregation characteristics, and precipitated phase distribution within the defect regions, aiming to reveal the microstructural differences between the defect regions and the matrix.

The sampling location for the segregation channel region of Freckle-II on Casting B is shown in Figure 6(a), and the corresponding metallographic structure of the cross-section A-A is presented in Figure 6(b). Figures 6(c) and (d) show the locally enlarged structures of the regions marked by the blue and red boxes in Figure 6(b), respectively. As shown in Figures 6(b)-(d), significant asymmetric microstructural characteristics are observed on the blade cross-section: the outer surface of the convex side exhibits a continuous and densely distributed eutectic layer, indicating solute enrichment during solidification; in contrast, the inner surface of the suction side shows relatively depleted eutectic structures, with the area fraction of interdendritic eutectic regions being significantly lower than that on the outer surface. Furthermore, no distinct grain boundaries are observed between the segregation channel of Freckle-II and the surrounding matrix.

The aforementioned microstructural differences between the convex side and the concave side indicate that the formation of segregation channels is closely related to the asymmetric heating conditions during solidification. The convex side, facing the cold zone, experiences a slower solidification rate, allowing sufficient solute enrichment and the formation of a continuous eutectic layer. In contrast, the concave side, facing the hot zone, undergoes faster solidification with more complete solute diffusion, resulting in a relatively depleted eutectic layer. Essentially, the segregation channel is a eutectic concentration zone formed by solute enrichment, and its unique microstructure lays the compositional foundation for the subsequent nucleation and evolution of stray grains.

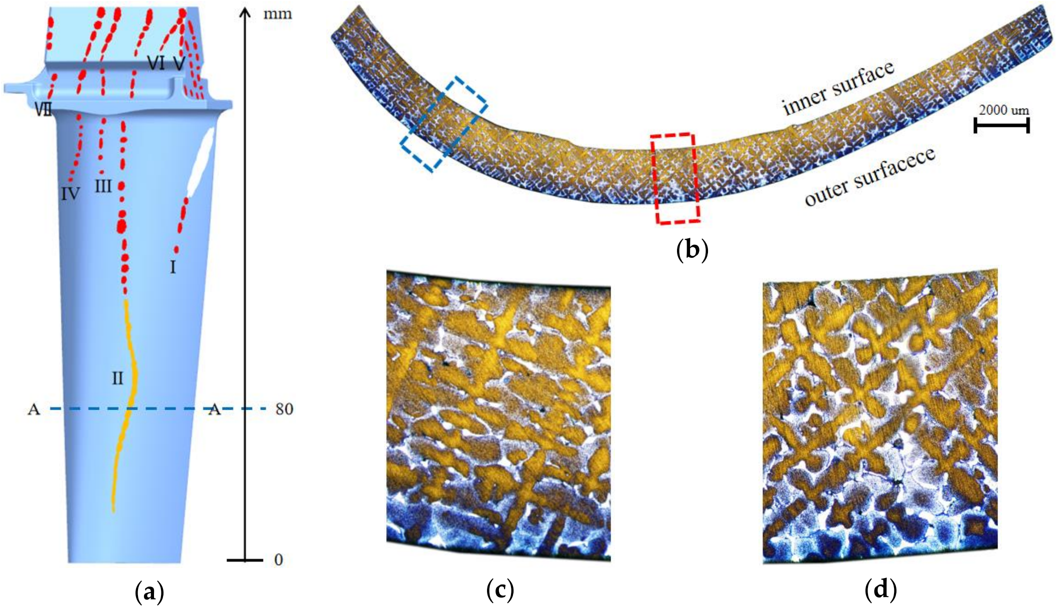

(b)

(a) (c) (d)

Figure 6. Metallographic characteristics of the segregation channel region of Freckle-II on Casting B: (**a**) Schematic diagram of the sampling position on section A-A; (**b**) Metallographic structure of section A-A; (**c**) Metallographic structure of the area marked by the blue box in (b); (**d**) Metallographic structure of the area marked by the red box in (b).

3.2.2. Transition from Segregation Channel to Stray Grains in Freckle-II

The sampling positions for the transition region between the segregation channel and stray grains of Freckle-II on Casting B are shown in Figures 7(a) and (b), and the corresponding metallographic structure of the longitudinal section is presented in Figure 7(c). Analysis of Figure 7(c) reveals significant microstructural characteristics on the blade longitudinal section: the lower region adjacent to the segregation channel retains a substantial amount of eutectic-rich structure; after transitioning toward the upper part of the airfoil, isolated fine stray grains gradually form and progressively increase in the amount of stray grains with the increasing height, with clearly visible grain boundaries. This microstructural transformation confirms the incubation and formation process of freckle defects, namely the stepwise evolution mechanism from solute segregation accumulation forming eutectic channels to eutectic convection disrupting dendrites and evolving into stray grains.

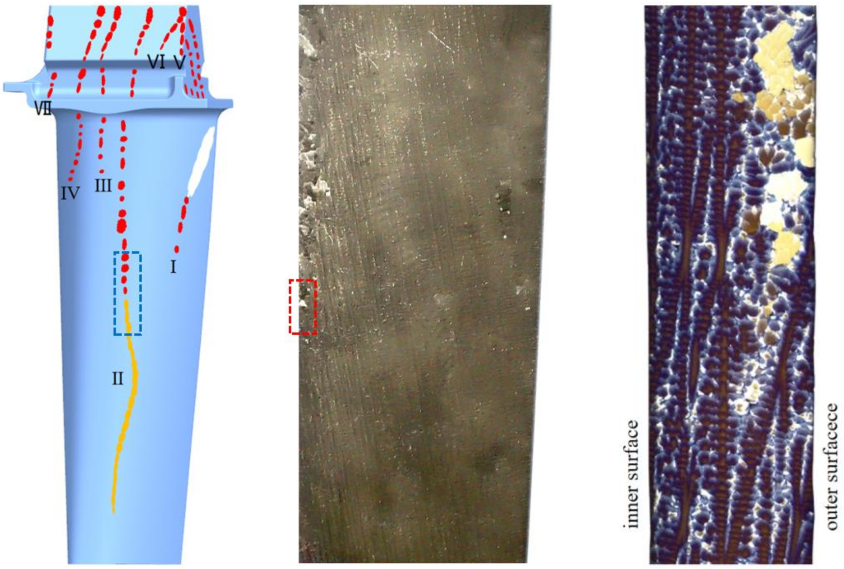

(a) (b) (c)

Figure 7. Metallographic characteristics of the transition region between the segregation channel and stray grains of Freckle-II on Casting B: (**a**) Schematic diagram of the sampling position on the convex side; (**b**) Enlarged image of the area marked by the blue box in (a); (**c**) Metallographic structure of the area marked by the red box in (b).

3.2.3. Metallographic Characteristics of the Freckle-VI Region

The metallographic structure of the Freckle-VI region on Casting B is shown in Figure 8. Located above the platform, this region represents the direct initiation site of freckle defects. In contrast to the segregation channel and transition region of Freckle-II, its microscopic morphology exhibits significant differences: the entire region lacks distinct incubation characteristics of segregation channels, with defects primarily characterized by isolated stray grains. Regarding the distribution and evolution of stray grains, this region displays a pronounced longitudinal variation. The bottom of the initiation zone is dominated by fine, irregularly dispersed stray grains appearing as dotted patterns. As the solidification height increases, the stray grains gradually coarsen, evolving into large blocky grains in the upper part of the region, with clearly visible grain boundaries. This evolutionary sequence indicates that the formation of Freckle-VI also undergoes a dynamic process from onset to further development, albeit without experiencing an obvious segregation channel incubation stage.

The above characteristics indicate that the formation mechanism of Freckle-VI differs from that of Freckle-II. Its initiation is primarily associated with flow disturbances caused by the abrupt cross-sectional change above the platform. Due to the relatively weak local solute segregation, the conditions for forming a continuous eutectic layer are not met, consequently exhibiting a microstructure dominated by stray grains.

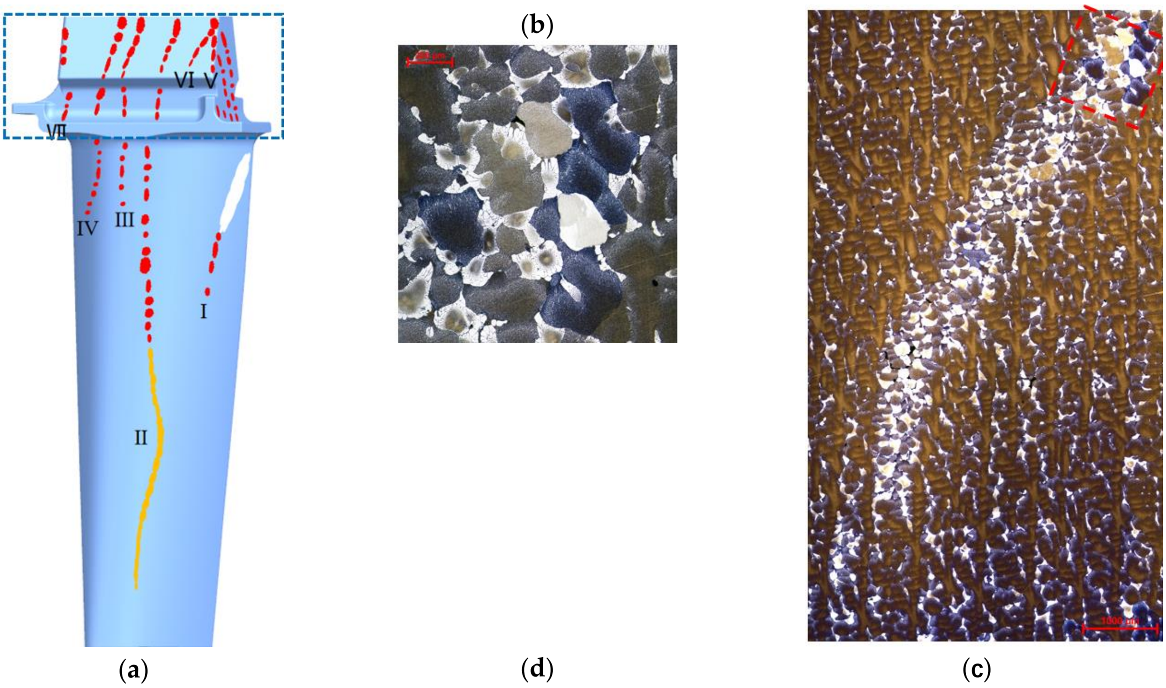

Figure 8. Metallographic characteristics of the entire Freckle-VI region on Casting B: (**a**) Schematic diagram of the sampling position; (**b**) Physical image of the area marked by the blue box in (a); (**c**) Metallographic structure of the area marked by the red box in (b); (**d**) Enlarged view of the metallographic structure in the area marked by the red box in (c)

4. Solidification Simulation and Freckle Formation Analysis

4.1. Correlation Analysis Between Solidification Process Characteristics and Freckle Formation

4.1.1. Criteria for Freckle Formation

Since the formation of freckle defects originates from the flow behavior of the interdendritic liquid, researchers have also attempted to reveal their formation mechanism by establishing fluid dynamics models. Within this research framework, the Rayleigh number (*Ra*) and its variants are commonly employed to characterize the stability of interdendritic liquid flow within the mushy zone [23,37–39]. For instance, the Rayleigh number criterion proposed by Auburtin et al. [37] is expressed as:

$$Ra = \frac{\Delta\rho}{\rho_0}\frac{gKh}{\alpha v} \tag{1}$$

where ρ_0 is the initial density (kg/m³); $\Delta\rho$ is the density variation (kg/m³); g is the gravitational acceleration (m/s²); h is the mushy zone width (m); α is the thermal diffusivity (m²/s); ν is the kinematic viscosity (m²/s); and K is the average permeability (m²).

The average permeability K is calculated using the following expression[40]:

$$K = 3.75\times10^{-4} f_L^2 \lambda_1^2 \tag{2}$$

Where f_L is the liquid fraction, and λ_1 is the primary dendrite arm spacing (μm).

The primary dendrite arm spacing is related to the solidification conditions and can be calculated by the following equation[40]:

$$\lambda_1 = C\times G_T^{-m} V^{-n} \tag{3}$$

where G_T is the temperature gradient (K/mm), V is the solidification rate (μm/s), and C, m, n are material constants related to the alloy composition, all greater than 0. For example, Guo et al. [41]

determined the relevant constants for the DD8 alloy through experiments as: $C = 1114.5$, $m = 0.52$, $n = 0.12$.

The aforementioned Rayleigh number essentially represents the ratio of the driving force for upward liquid flow to the resistance within the mushy zone. When Ra in a certain region exceeds the critical value Ra^* during solidification, it can be determined that freckle defects will initiate at that location. This critical value can be determined through theoretical calculations or experimental measurements.

4.1.2. Analysis of Freckle Formation Mechanism in Castings at Different Furnace Positions

Third-generation nickel-based single crystal superalloys contain high concentrations of refractory elements such as Re and W, exhibiting severe microsegregation behavior during solidification: high-melting-point, high-atomic-weight elements like Re and W tend to segregate to the dendrite cores, while low-density, eutectic-forming elements such as Al and Ta preferentially enrich in the interdendritic liquid [3]. This pronounced elemental segregation leads to two critical consequences: first, the interdendritic liquid becomes enriched with low-density elements (Al, Ta), resulting in density inversion that provides the driving force for thermosolutal convection; second, the solidification interval (the temperature difference between liquidus and solidus) increases significantly, forming a wide mushy zone that provides the spatial conditions for convection and dendrite fragmentation.

Macroscopic observations indicate that freckle defects on the convex side outer surface of Casting B (cold zone casting) are significantly more severe than those of Casting A (hot zone casting) in terms of distribution range, number density, and morphological complexity. This difference arises from the distinct temperature fields and solidification conditions experienced by the two castings due to their different positions within the furnace.

Figure 9 presents the calculated solidification progression of the castings at $t = 4500$ s. It can be seen that at the same moment, Casting B (cold zone) exhibits faster solidification progression and a wider mushy zone, whereas Casting A (hot zone) shows slower solidification progression and a narrower mushy zone. Figure 10 shows the calculated temperature gradient distribution within the blade castings during solidification when the casting temperature drops to $T = 1396.37$ °C (solid fraction $f_s = 50\%$). At the same solidification height, the temperature gradient of Casting A is approximately twice that of Casting B.

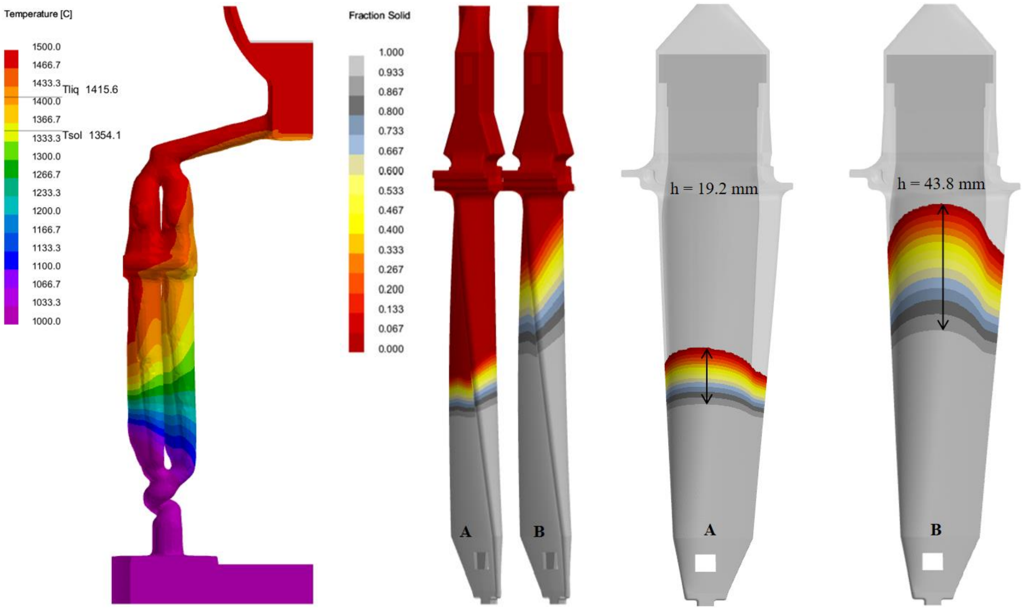

(**a**) (**b**) (**c**) (**d**)

Figure 9. Simulated solidification results of castings at $t = 4500$ s: (**a**) Temperature field distribution of the ceramic shell; (**b**) Solidification height of the castings; (c) Mushy zone height of Casting A; (**d**) Mushy zone height of Casting B.

According to the Rayleigh number model formula (1), a larger mushy zone width h leads to a larger Rayleigh number Ra, resulting in a higher susceptibility to freckle defects. Furthermore, based on the primary dendrite arm spacing formula (3), a smaller temperature gradient G_T results in a larger primary dendrite arm spacing λ_1, which in turn increases the average permeability K (see formula (2)), thereby further elevating the Ra value. Consequently, Casting B exhibits a significantly larger Rayleigh number than Casting A due to its wider mushy zone and smaller temperature gradient, which fundamentally accounts for the markedly greater severity of freckle defects in Casting B compared to Casting A.

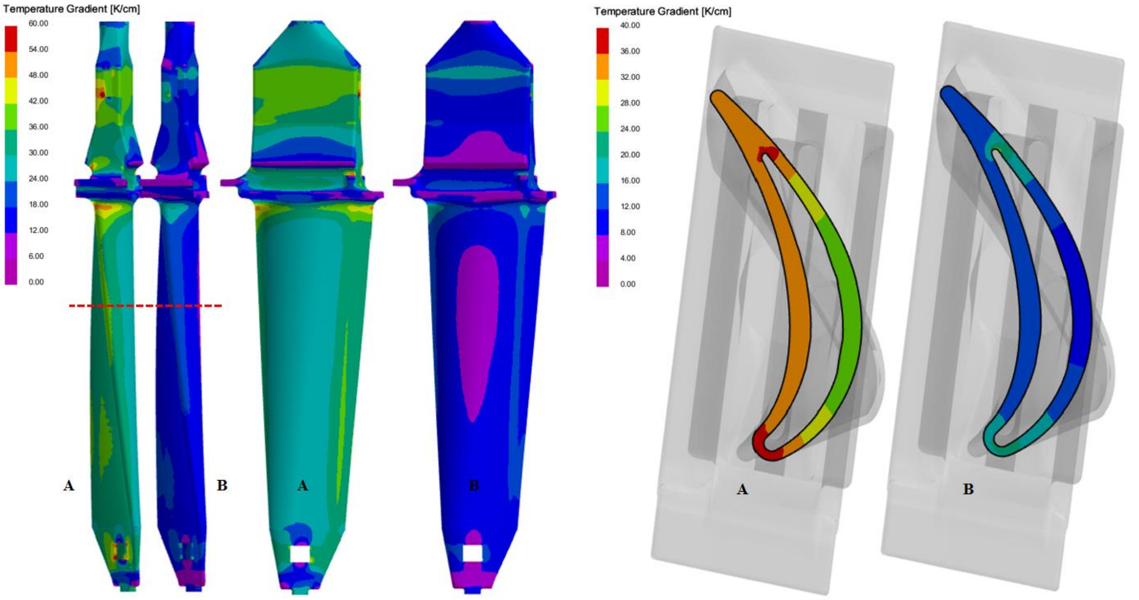

(**a**) (**b**)

Figure 10. Calculated temperature gradient distribution during solidification at $T = 1396.37$ °C (solid fraction $f_s = 50\%$): (**a**) Temperature gradient distribution on the outer surface of Castings A and B; (**b**) Temperature gradient distribution on the cross-section (the read dash line in (a)) of Castings A and B.

4.1.3. Analysis of Freckle Defect Distribution Differences Between the Concave Side and Convex Side of the Same Casting

Macroscopic observations indicate significant differences in freckle defect distribution on different sides of the same casting. Taking Casting B as an example, the convex side exhibits severe freckle defects characterized by wide distribution range, high number density, and diverse morphologies, while the concave side surface remains clean, with virtually no freckle defects or obvious segregation traces. This difference originates from the distinctly different temperature fields and solidification conditions experienced by different sides of the casting within the furnace.

Figure 11 presents the simulated solidification progression of Casting B at $t = 4500$ s. It can be observed that at the same moment, the convex side, being adjacent to the cold zone, exhibits faster solidification progression and a wider mushy zone, whereas the concave side, situated close to the hot zone and receiving intense thermal radiation from the heating wall, shows slower solidification progression and a narrower mushy zone. Figure 12 displays the calculated temperature gradient distribution during solidification when the casting temperature drops to $T = 1396.37$ °C (solid fraction $f_s = 50\%$). At the same solidification height, the temperature gradient on the concave side is larger than that on the convex side.

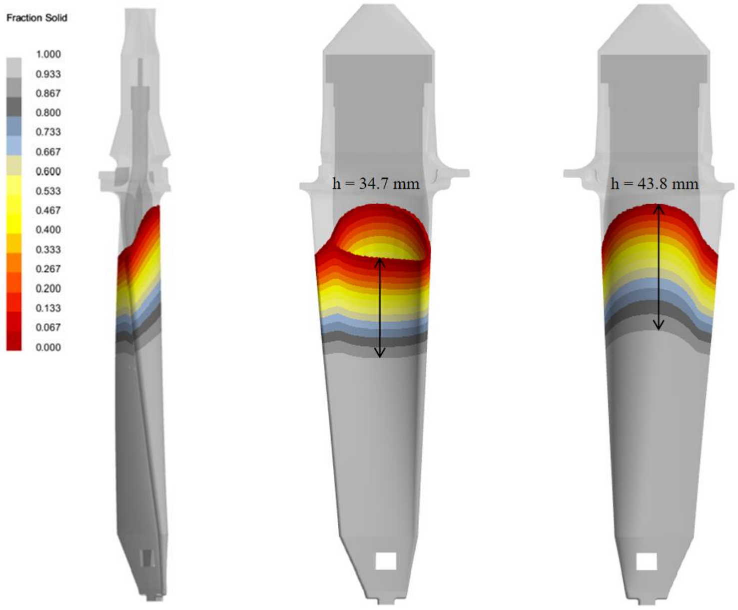

(**a**) (**b**) (**c**)

Figure 11. Calculated solidification results of Casting B at t = 4500 s: (**a**) Solidification height of the casting; (**b**) Mushy zone height on the concave side; (**c**) Mushy zone height on the convex side.

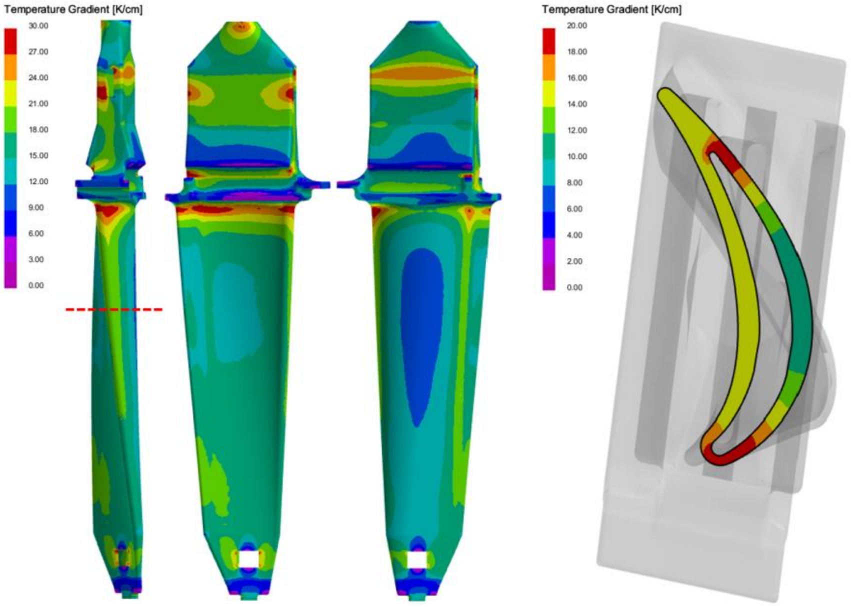

(**a**) (**b**)

Figure 12. Calculated temperature gradient distribution during solidification of Casting B at T = 1396.37 °C (solid fraction f_s = 50%): (**a**) Temperature gradient distribution on the outer surface of Casting B; (**b**) Temperature gradient distribution on the cross-section (the read dash line in (a)) of Casting B.

According to the Rayleigh number model formula (1) and the primary dendrite arm spacing formula (3), the convex side, characterized by a wider mushy zone and a smaller temperature gradient, exhibits a significantly larger Rayleigh number than the concave side. Furthermore, a portion of the solute from the concave side can migrate to the convex side through convection, further reducing its own segregation tendency. Consequently, the concave side surface remains largely free of freckle defects and segregation channels, while the convex side shows a substantially higher severity of freckle defects. In summary, the pronounced difference in freckle defect distribution between the convex side and concave side of Casting B results from the coupled effects of temperature field and solidification behavior under asymmetric heating conditions.

4.2. The Formation Mechanism of Freckle Defects and Model Validation

4.2.1. Formation Mechanism of Freckles

During directional solidification, light solute elements are rejected at the solid–liquid interface, leading to progressive enrichment of solute in the interdendritic liquid within the mushy zone. As solidification proceeds, the solute concentration of the interdendritic liquid increases with the depth of the mushy zone, resulting in a density inversion in which the lower part of the mushy zone contains lighter liquid. This density instability induces thermo-solutal convection and promotes the formation of channel segregation [36]. As shown in Figure 13(a), the low-density solute-enriched liquid rises within the mushy zone and develops into segregation channels. The upward flow continuously entrains surrounding solute-rich interdendritic liquid into the channel, thereby sustaining and intensifying the channel flow. When the flow intensity becomes sufficiently strong, the higher-order dendrite arms near the channel are remelted and fragmented, leading to the formation of stray grains[28]. After complete solidification, freckles appear macroscopically as regions of local eutectic enrichment accompanied by dispersed misoriented stray grains.

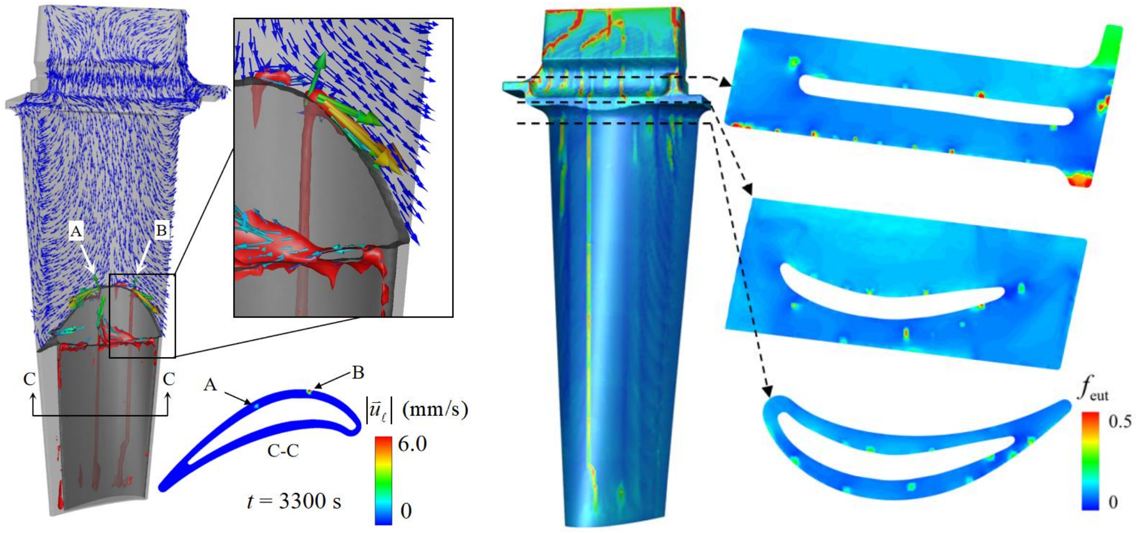

(**a**) (**b**)

Figure 13. The flow and solidification of the turbine blade casting. (**a**) The onset of freckles. The red isosurfaces represent plumes ahead of the solidification front and segregation channels within the mushy zone below the front. The thin blue vectors on the convex surface indicate the flow direction in the bulk liquid, whereas the thick colored vectors denote the liquid velocity within the plumes and channels. A horizontal section (C–C) is also shown to illustrate the positions of the segregation channels (Reprinted from reference,[36] under the terms of the Creative Commons CC BY license). (**b**) Distribution of freckle defects on the outer surface of Casting B.

The calculated freckle distribution is presented in Figure 13(b). Multiple freckles are predicted on the convex side of the blade, and their severity increases toward the upper part of the airfoil, which agrees well with the experimental observations shown in Figure 5. To further analyze the spatial evolution of freckles, three horizontal sections located below the platform, within the platform, and above the platform were examined. As illustrated in Figure 13(b), the segregation channels formed below the platform penetrate through the platform region and immediately develop into freckles above it. This simulation result explains the experimental observations in Figures 5 and 8, where freckles are observed below the platform, disappear on the platform surface, and reappear immediately above the platform. These results indicate that freckle formation is a continuous process governed by the coupled effects of interdendritic flow and solute transport during solidification.

Figure 14 presents a comparison between the simulated and experimental results of freckle defect distribution on different regions of the outer surface of Casting B. As shown in Figure 14(a), for the convex side of the turbine blade, although the simulation did not exactly replicate every individual segregation channel marked as Freckles I–VII, it successfully captured the overall distribution trend of the freckle defects. Figures 14(b) and (c) illustrate the comparison of freckle distribution on the right and left sides of the fir-tree root, respectively. The simulation results accurately reproduced the number and positions of the freckles observed in the experiments. In summary, the simulation and experimental results are in good agreement.

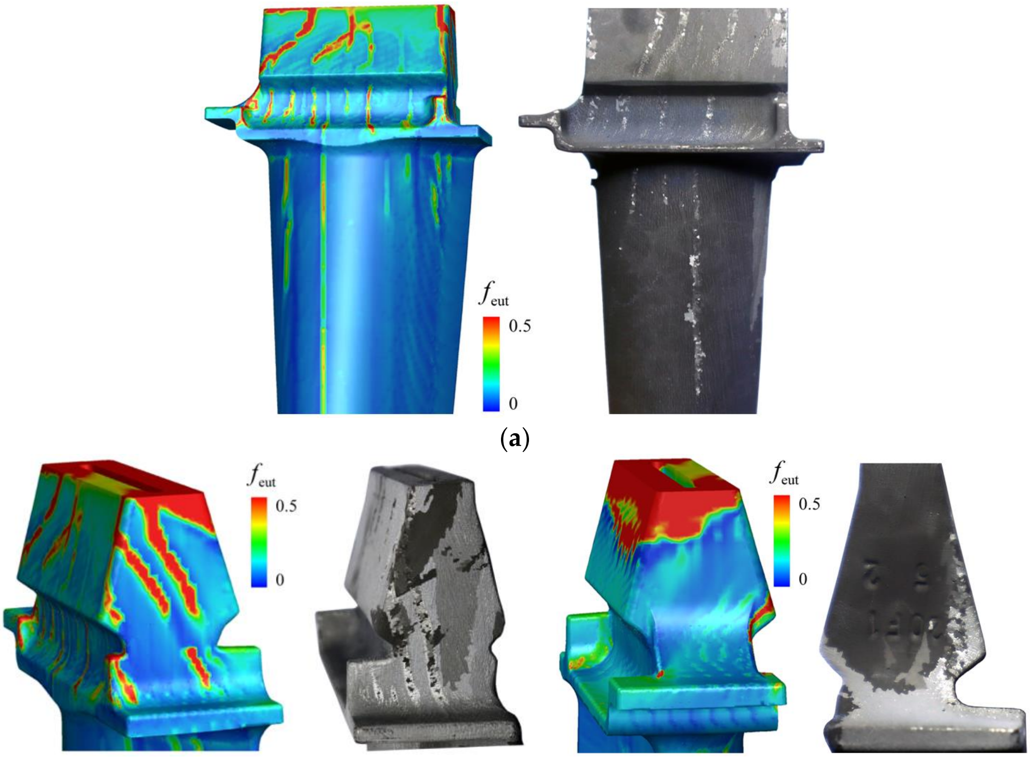

(**a**)

(**b**) (**c**)

Figure 14. Comparison of simulated and experimental freckle defect distributions on the outer surface of Casting B: (**a**) Convex side; (**b**) Right side of the fir-tree root; (**c**) Left side of the fir-tree root.

On the concave side, the freckle defects predicted by the simulation were not observed experimentally. This discrepancy may result from the combined effects of numerical and experimental factors. As discussed in Section 4.1.3, the solidification front on the convex side is a preferential site for freckle initiation. However, the neglect of liquid flow in the ProCAST thermal calculation may overestimate the mushy zone height on the concave side, thereby affecting the accuracy of defect prediction.

In addition, during the actual directional solidification process, the ceramic core is prone to eccentricity, leading to uneven wall thickness distribution of the blade. If the ceramic core shifts slightly toward the concave side, the local wall thickness on the convex side becomes slightly greater than that on the concave side. Such geometric deviation may further enhance the melt flow intensity in the convex side region, consequently influencing the actual distribution of freckle defects.

4.2.2. Comparison of Simulated and Experimental Freckles Distribution on the Cross-Section

Figure 15 presents a comparison between the simulated and experimental results of freckle defect distribution on the casting cross-section near the platform. As shown in Figure 15(b), for the turbine blade cross-section, although the simulation did not exactly replicate every individual segregation channel, it successfully captured the overall distribution trend of the freckle defects.

Furthermore, as shown in Figure 15(b), freckle defects are observed not only on the outer surface of the convex side (Surface B2) but also on the inner surface of the concave side (Surface A2). This finding differs from the observations in previous sections, where freckle defects were found to be distributed only on the outer surface of the casting. It is worth noting that both the simulation and

doi:10.20944/preprints202603.0714.v1

experimental results confirm the presence of freckle defects on the inner surface of the concave side, demonstrating good agreement between the two.

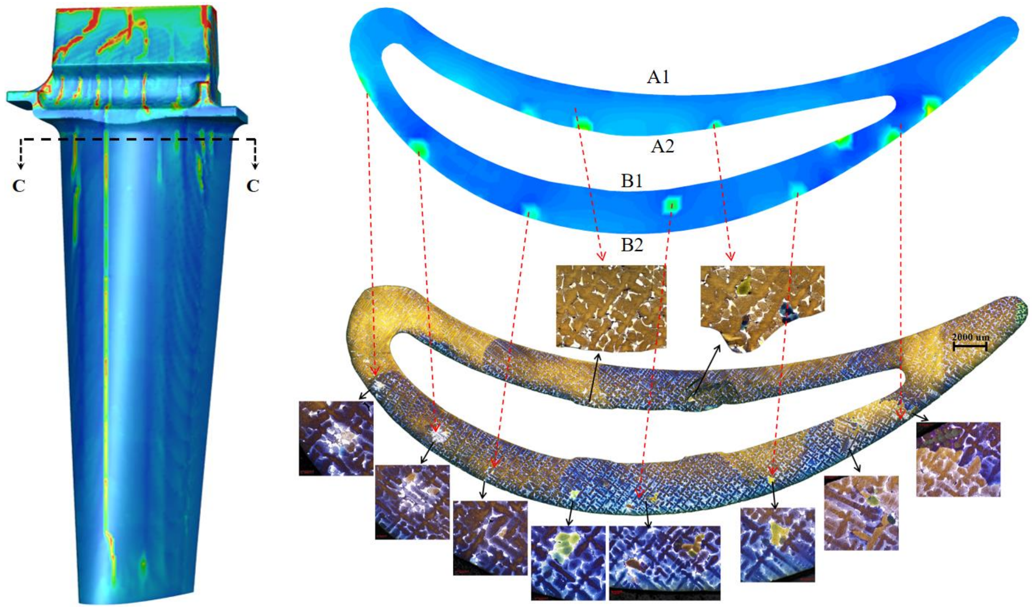

(**a**) (**b**)

Figure 15. Comparison of simulated and experimental freckle defect distributions on the casting cross-section: (**a**) Schematic diagram of the sampling position on section C-C; (**b**) Comparison of defect distributions on the cross-section C-C.

Referring to the analysis method in Section 4.1.3, a comparison of the solidification progress between the outer surface (Surface A1) and the inner surface (Surface A2) of the concave side reveals that at the same solidification moment, the mushy zone height on Surface A2 is larger than that on Surface A1; at the same height position, the temperature gradient on Surface A2 is smaller than that on Surface A1. According to the Rayleigh number model (Equation (1)) and the primary dendrite arm spacing formula (Equation (3)), a wider mushy zone and a smaller temperature gradient result in a larger Rayleigh number, indicating a higher susceptibility to freckle formation. Therefore, Surface A2 is more prone to freckle defects than Surface A1, which mechanistically explains the appearance of freckle defects on the inner surface of the concave side. This finding is consistent with the results reported in the literature [42] and holds significant guiding importance for optimizing the directional solidification process of third-generation nickel-based single crystal superalloys.

5. Conclusions

(1) The formation mechanism of freckle defects during the directional solidification of a third-generation nickel-based single crystal superalloy turbine blade has been elucidated. Freckle formation originates from severe microsegregation caused by high concentrations of refractory elements (Re, W, Ta, etc.), which induces density inversion in the interdendritic liquid and the development of a wide mushy zone. Under the influence of thermo-solutal convection, dendrites undergo fragmentation and aggregate into equiaxed grain chains, ultimately evolving into surface chain-like freckle defects.

(2) The critical role of casting position in determining freckle defect distribution has been clarified. Casting B, positioned farther from the heat source, exhibits a substantially larger Rayleigh number than Casting A (located closer to the heat source), due to its lower temperature gradient and wider mushy zone. Consequently, freckle defects in Casting B are significantly more severe in terms of distribution range, number density, and morphological complexity. The strong agreement between simulation results and experimental observations confirms the decisive influence of thermal field and solidification conditions on freckle formation.

(3) The underlying causes of the asymmetric freckle distribution on opposite sides of the same casting have been identified. The suction side, being farther from the heat source, is characterized by a wider mushy zone and a smaller temperature gradient, resulting in a Rayleigh number substantially higher than that of the pressure side. This explains the severe freckling observed on the suction side, while the pressure side, benefiting from its proximity to the heat source, remains virtually defect-free.

(4) The accuracy and reliability of the volume-averaged multiphase solidification model for predicting freckle defects have been validated. The simulation successfully reproduced the overall distribution trends of freckle defects on both the outer surface and cross-section of Casting B, achieving good consistency with experimental results. Notably, both simulation and experiments confirmed the presence of freckle defects not only on the outer surface of the suction side but also on the inner surface of the pressure side, a finding that broadens the current understanding of freckle distribution patterns.

(5) The susceptibility to freckle formation varies with blade geometry. The airfoil region exhibits a relatively lower susceptibility, requiring an incubation stage involving segregation channels before freckles develop. In contrast, the fir-tree root region shows severe freckle defects, characterized by high quantity and direct formation without a segregation channel incubation stage. This is attributed to the fir-tree root being a thick-walled section located in the upper part of the casting, where both the temperature gradient and solidification rate are low.

(6) The established "global-local" two-step digital twin strategy has successfully enabled cross-scale coupling calculations between macroscopic thermal fields and microstructural evolution. This provides a feasible technical pathway for the digital manufacturing of turbine blades and offers significant guidance for optimizing directional solidification processes and achieving active defect control.

Author Contributions: X.L.: conceptualization, methodology, software, data curation, investigation, visualization, writing—original draft preparation; A.L.: investigation, data curation; H.Z.: methodology, formal analysis; D.M.: writing—review & editing, supervision; M.S.: writing—review & editing, super-vision; M.W.:writing—review & editing, supervision; J.G.: methodology, investigation, writ-ing—review & editing, funding acquisition, supervision, project administration. All authors have read and agreed to the published version of the manuscript.

Funding: This work was supported by Advanced Materials-National Science and Technology Major Project, China (Nos. 2025ZD0608600).

Data Availability Statement: The original contributions presented in the study are included in the article, further inquiries can be directed to the corresponding authors.

Conflicts of Interest: The authors declare no conflicts of interest.

References

1. Zhang, J.; Wang, L.; Wang, D.; Xie, G.; Lu, Y.Z.; Shen, J.; Lou, L.H. Recent Progress in Research and Development of Nickel-Based Single Crystal Superalloys. Acta Metallurgica Sinica, 2019, 55(9): 1077-1094. DOI:10.11900/0412.1961.2019.00122
2. Zhou, Y.; Zhao, X.; Fan, Y.; Yue, Q.; Xia, W.; Pan, Q.; Cheng, Y.; Li, W.; Gu, Y.; Zhang, Z. Composition Optimization in Alloy Design for Nickel-Based Single Crystal Superalloy: A Review. Metals 2025, 15, 793. https://doi.org/10.3390/met15070793
3. Zhao, Y.X.; Ma, D.X.; Wie, J.H.; Yuan, Y.Y.; Xu, W.T.; Li, L.; Deng, Y.P. Study on solidification microstructure of a third generation single crystal superalloy WZ30. Journal of Central South University (Science and Technology), 2025, 56(2): 478-486. DOI: 10.11817/j.issn.1672-7207.2025.02.007.
4. Jia, Y.; Zhang, Y.; Wang, S. Cheng, F.; Shi, C.K.; Shi, Z.K. Constitutional Supercooling-induced Freckle Nucleation Mechanism of Nickel-based Superalloy During Directional Solidification. Metall Mater Trans A 56, 2202–2214 (2025). https://doi.org/10.1007/s11661-025-07750-3

5. Wang, Z.C.; Li, J.R.; Liu, S.Z.; Yang, W.P. Microstructural Characteristics of Freckles in Ni-based Single Crystal Superalloys. Rare Metal Materials and Engineering, 2022, 51(10):3533~3541. DOI:10.12442/j.issn.1002-185X.20210889
6. Seo, S.M.; Lee, J.H.; Yoo, Y.S.; Jo, C.Y.; Miyahara, H.; Ogi, K. A Comparative Study of the γ/γ′ Eutectic Evolution During the Solidification of Ni-Base Superalloys. Metallurgical and Materials Transactions A, 2011: 3150-3159. http://dx.doi.org/10.1007/s11661-011-0738-4. DOI:10.1007/s11661-011-0738-4.
7. Aveson, J. W.; Reinhart, G.; Goddard, C. J. L.; Nguyen-Thi, H.; Mangelinck-Noël, N. Tandjaoui, A.; Davenport, J.R.; Warnken, N.; Gioacchino, F.D.; Lafford, T.A.; Souza, N.D.; Billia, B.; Stone, H.J. On the Deformation of Dendrites During Directional Solidification of a Nickel-Based Superalloy. Metallurgical and Materials Transactions A, 2019, 50, 5234-5241. https://doi.org/10.17863/CAM.56694
8. Brewster, G.; Dong, H.B.; Green, N.R.; D'Souza, N. Surface Segregation during Directional Solidification of Ni-Base Superalloys. Metallurgical and Materials Transactions B, 2008: 87-93. http://dx.doi.org/10.1007/s11663-007-9118-2. DOI:10.1007/s11663-007-9118-2.
9. Cao, L.; Yao, L.; Zhou, Y.Z; Jin, T.; Sun, X.F. Formation of the Surface Eutectic of a Ni-based Single Crystal Superalloy. Journal of Materials Science & Technology, 2017: 347-351. http://doi.org/10.1016/j.jmst.2016.08.014.
10. Copley, S.M.; Giamei, A.F.; Johnson, S.M.; Hornbecker, M. F. The origin of freckles in unidirectionally solidified castings. Metall Trans 1, 2193–2204 (1970). https://doi.org/10.1007/BF02643435
11. Versnyder, F.I.; Shank, M.E. The development of columnar grain and single crystal high temperature materials through directional solidification. Materials Science and Engineering, 1970, 6(4):213-247. DOI:10.1016/0025-5416(70)90050-9.
12. Giamei, A.F.; Kear, B.H. On the nature of freckles in nickel base superalloys. Metallurgical and Materials Transactions B, 1970, 1(8):2185-2192. DOI:10.1007/BF02643434.
13. Auburtin, P.; Wang, T.; Cockcroft, S. L.; Mitchell, A. Freckle formation and freckle criterion in superalloy castings. Metallurgical & Materials Transactions B, 2000, 31(4):801-811. DOI:10.1007/s11663-000-0117-9.
14. Ma, D.X.; Bührig-Polaczek, A. The Geometrical Effect on Freckle Formation in the Directionally Solidified Superalloy CMSX-4. Metall Mater Trans A 45, 1435–1444 (2014). https://doi.org/10.1007/s11661-013-2088-x
15. 33.Ren, N.; Panwisawas, C.; Li, J.; Xia, M.X.; Dong, H.B; Li, J.G. Solute enrichment induced dendritic fragmentation in directional solidification of nickel-based superalloys, Acta Materialia, Volume 215,2021,117043. https://doi.org/10.1016/j.actamat.2021.117043.
16. Sarazin, J.R.; Hellawell, A. Channel formation in Pb-Sn, Pb-Sb, and Pb-Sn-Sb alloy ingots and comparison with the system NH4CI-H2O. Metall Trans A 19, 1861–1871 (1988). https://doi.org/10.1007/BF02645156
17. Hellawell, A.; Sarazin, J. R.; Steube, R. S. Channel Convection in Partly Solidified Systems. Philos Trans A Math Phys Eng Sci 15 December 1993; 345 (1677): 507–544. https://doi.org/10.1098/rsta.1993.0143
18. Hellawell, A.; Liu, S.; Lu, S.Z. Dendrite fragmentation and the effects of fluid flow in castings. JOM 49, 18–20 (1997). https://doi.org/10.1007/BF02914650
19. Pollock, T.M.; Murphy, W.H. The breakdown of single-crystal solidification in high refractory nickel-base alloys. Metall Mater Trans A 27, 1081–1094 (1996). https://doi.org/10.1007/BF02649777
20. Copley, S.M.; Giamei, A.F.; Johnson, S.M.; Hornbecker, M. F. The origin of freckles in unidirectionally solidified castings. Metall Trans 1, 2193–2204 (1970). https://doi.org/10.1007/BF02643435
21. Han, D.Y.; Jiang, W.G.; Xiao, J.H.; Li, K.W.; Lu, Y.Z.; Lou, L.H. Influence of Geometric Structure and Feeding Behavior of Casting on Freckle Formation during Directional Solidification of a Ni-Based Single-Crystal Superalloy. Crystal Research and Technology: Journal of Experimental and Industrial Crystallography, 2021(5):56. https://doi.org/10.1002/crat.202000197
22. Ma, D.X.; Dong, Z.H.; Wang, F; Dong H. B. A Phenomenological Analysis of Freckling in Directional Solidification of Ni-Base Superalloy: The Role of Edge and Curvature in Casting Components. Metall Mater Trans A 51, 88–92 (2020). https://doi.org/10.1007/s11661-019-05513-5
23. Ma, D. X.; Mathes, M.; Zhou, B.; Bührig-Polaczek, A. Influence of Crystal Orientation on the Freckle Formation in Directionally Solidified Superalloys. Advanced Materials Research, 2011, 278:114-119. DOI: 10.4028/www.scientific.net/AMR.278.114.

24. Beckermann, C.; Gu, J.P.; Boettinger, W. J. Development of a freckle predictor via rayleigh number method for single-crystal nickel-base superalloy castings. Metallurgical & Materials Transactions A, 2000, 31(10):2545-2557.DOI:10.1007/s11661-000-0199-7
25. Guo, J.Z.; Beckermann, C. Three-Dimensional Simulation of Freckle Formation during Binary Alloy Solidification: Effect of Mesh Spacing. Numerical Heat Transfer, 2003, 44(6):559-576.DOI:10.1080/716100512.
26. Takaki, T.; Ohno, M.; Shimokawabe, T.; Aoki, T. Two-dimensional phase-field simulations of dendrite competitive growth during the directional solidification of a binary alloy bicrystal. Acta Materialia, 2014, 81:272–283.https://doi.org/10.1016/j.actamat.2014.08.035.
27. Yuan, L.; Lee, P.D. A new mechanism for freckle initiation based on microstructural level simulation. Acta Materialia, 2012, 60(12):4917-4926. https://doi.org/10.1016/j.actamat.2012.04.043.
28. Zhang, H.; Zhao, Y.; Xiong, W.; Ma, D.; Ludwig, A.; Kharicha, A.; Wu, M. Modelling freckles and spurious grain formation in directionally solidified superalloy castings. Commun Mater 5, 232 (2024). https://doi.org/10.1038/s43246-024-00672-4
29. Ren, N.; Li, J.; Panwisawas, C.; Xia, M.X.; Dong, H.B.; Li, J.G. Thermal-solutal-fluid flow of channel segregation during directional solidification of single-crystal nickel-based superalloys. Acta Materialia, 2021, 206. https://doi.org/10.1016/j.actamat.2020.116620.
30. Schneider, M.C.; Gu, J.P.; Beckermann, C.; Boettinger, W.J.; Kattner, U.R. Modeling of micro- and macrosegregation and freckle formation in single-crystal nickel-base superalloy directional solidification. Metall Mater Trans A 28, 1517–1531 (1997). https://doi.org/10.1007/s11661-997-0214-3
31. Ren, N.; Li, J.; Panwisawas, C.; Xia, M.X.; Dong, H.B.; Li, J.G. Insight into the sensitivities of freckles in the directional solidification of single-crystal turbine blades. Journal of Manufacturing Processes, 2022 77:219-228. https://doi.org/10.1016/j.jmapro.2022.03.019
32. Ma, D.; Wu, Q.; Bührig-Polaczek, A. Some New Observations on Freckle Formation in Directionally Solidified Superalloy Components. Metall Mater Trans B 43, 344–353 (2012). https://doi.org/10.1007/s11663-011-9608-0
33. Schadt, R.; Wagner, I.; Preuhs, J.; Sahm, P.R. New Aspects of Freckle Formation During Single Crystal Solidification of CMSX-4. Miner. Met. Mater. Soc. TMS (2000) 211 218. https://doi.org/10.7449/2000/superalloys_2000_211_218.
34. Kaewchoothong, N.; Maliwan, K.; Nuntadusit, C. Numerical simulations on flow and heat transfer in ribbed two-pass square channels under rotational effects, IOP Conf. Ser. Mater. Sci. Eng. 243 (2017), 012004, https://doi.org/10.1088/1757-899X/243/1/012004.
35. Xu, W; Wang, F.; Ma, D.; Zhu, X.; Li, D.; Bührig-Polaczek, A. Sliver defect formation in single crystal Ni-based superalloy castings – ScienceDirect. Materials & Design, 2020, 196, 109138. https://doi.org/10.1016/j.matdes.2020.109138.
36. Zhang, H.J.; Liu, X.S.; Ma, D.X.; Song, M.; Ludwig, A.; Kharicha, A.; Wu, M.H. Digital twin for directional solidification of a single-crystal turbine blade. Acta Materialia, 2023, 244, 118579. https://doi.org/10.1016/j.actamat.2022.118579.
37. Auburtin, P.; Wang, T.; Cockcroft, S.L. Mitchell, A. Freckle formation and freckle criterion in superalloy castings. Metall Mater Trans B 31, 801–811 (2000). https://doi.org/10.1007/s11663-000-0117-9
38. Yang, W.; Chang, K.M.; Chen, W.; Mannan, S.; DeBarbadillo, J. Freckle criteria for the upward directional solidification of alloys. Metall Mater Trans A 32, 397–406 (2001). https://doi.org/10.1007/s11661-001-0271-y
39. Tewari, S.N.; Tiwari, R.; Magadi, G. Mushy-zone rayleigh number to describe macrosegregation and channel segregate formation during directional solidification of metallic alloys. Metall Mater Trans A 35, 2927–2934 (2004). https://doi.org/10.1007/s11661-004-0240-3
40. Böttger, B.; Seiz, A.; Sowa, R.; Berger, R.; Apel, M. Numerical prediction of primary dendrite arm spacing (PDAS), properties of the mushy zone, and freckle risk for various multicomponent Ni-base superalloys using the 3D-phase-field method. Computational Materials Science, 2024(236),112854. https://doi.org/10.1016/j.commatsci.2024.112854.
41. He, G.; Mao, X.M.; Fu, H.Z. Models for primary dendrite spacing and its verification in single crystal superalloy. Materials Science Progress, 1993, 7(6):467-472. DOI:10.1007/BF02943552.

42. Ma, D.X.; Zhao, Y.X.; Xu, W.T.; Li, Z.X.; Liu, S.F. Freckle Formation in Specially Shaped Castings of a Single Crystal Superalloy. Special Casting & Nonferrous Alloys, 2021, 41(11):1345-1349. DOI: 10.15980/j.tzzz.2021.11.005.